

Interfacial Unit-Dependent Catalytic Activity for CO Oxidation over Cerium Oxysulfate Cluster Assemblies

Megan C. Wasson,[#] Xingjie Wang,[#] Patrick Melix, Selim Alayoglu, Andrew T. Y. Wolek, Ian Colliard, Florencia A. Son, Haomiao Xie, Eric Weitz, Timur Islamoglu, May Nyman, Randall Q. Snurr, Justin M. Notestein, and Omar K. Farha^{*}



Cite This: <https://doi.org/10.1021/acsami.2c05937>



Read Online

ACCESS |

Metrics & More

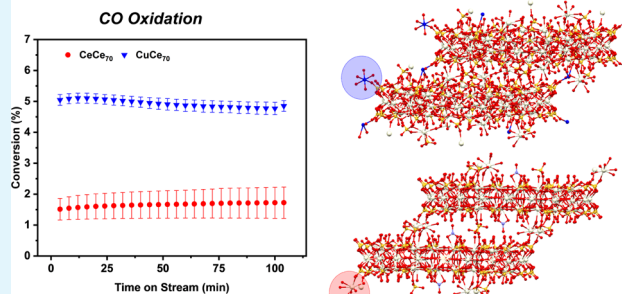
Article Recommendations

Supporting Information

ABSTRACT: Atomically precise cerium oxo clusters offer a platform to investigate structure–property relationships that are much more complex in the ill-defined bulk material cerium dioxide. We investigated the activity of the MCe_{70} torus family ($\text{M} = \text{Cd}, \text{Ce}, \text{Co}, \text{Cu}, \text{Fe}, \text{Ni}, \text{and Zn}$), a family of discrete oxysulfate-based Ce_{70} rings linked by monomeric cation units, for CO oxidation. CuCe_{70} emerged as the best performing MCe_{70} catalyst among those tested, prompting our exploration of the role of the interfacial unit on catalytic activity. Temperature-programmed reduction (TPR) studies of the catalysts indicated a lower temperature reduction in CuCe_{70} as compared to CeCe_{70} . *In situ* diffuse reflectance infrared Fourier transform spectroscopy (DRIFTS) indicated that CuCe_{70} exhibited a faster formation of Ce^{3+} and contained CO bridging sites absent in CeCe_{70} . Isothermal CO adsorption measurements demonstrated a greater uptake of CO by CuCe_{70} as compared to CeCe_{70} . The calculated energies for the formation of a single oxygen defect in the structure significantly decreased with the presence of Cu at the linkage site as opposed to Ce. This study revealed that atomic-level changes in the interfacial unit can change the reducibility, CO binding/uptake, and oxygen vacancy defect formation energetics in the MCe_{70} family to thus tune their catalytic activity.

KEYWORDS: cerium clusters, gas-phase oxidation, oxygen defects, interfacial unit effects, heterogeneous catalysis

Interfacial Element Affects Reactivity of MCe_{70} Clusters



INTRODUCTION

Bulk metal oxides are essential to a range of industries where their tunable surface and electronic structure facilitate their use as heterogeneous catalysts, in biomedical devices, and as semiconductors.^{1–3} In recent years, efforts have shifted to capitalizing on surface atoms and how the change in a chemical environment, i.e., fewer nearest neighboring atoms, can increase their catalytic properties as compared to their bulk counterparts.⁴ Such strategies have included isolating a smaller nanooxide size regime to increase the amount of surface atoms or a specific morphology to access desired surface facets with higher surface energies to increase their catalytic activity.^{5,6} However, great care is needed to minimize the polydispersity in these systems to confidently assign structure–property relationships given the surface heterogeneity.⁷ Other emerging strategies to access nano-sized bulk oxides tailored in size or shape include the growth of nano-sized oxides with templating mesoporous materials⁸ or on substrates such as thin films.⁹ Another strategy to access discrete nanooxide materials is their incorporation into structural building units in highly ordered hybrid materials, such as metal–organic frameworks (MOFs).¹⁰ Shifting to a smaller size regime with discrete,

crystallographically defined clusters enables more confident assignments of structure–activity relationships.¹¹ Thus, it is imperative to expand and subsequently interrogate the available library of metal-oxo clusters.¹²

Of the well-studied metal oxides, metal-oxo clusters that resemble cerium dioxide present a fascinating platform for further research given the facile storage and release of oxygen within ceria to form reactive oxygen vacancy defects.¹³ Enabled by the favorable redox couple of $\text{Ce}^{4+}/\text{Ce}^{3+}$, surface O atoms can readily be abstracted depending on reaction conditions and directly participate in reactions through a Mars–Van Krevelen mechanism.^{14,15} Moreover, subsurface atoms can facilitate the transport of O vacancies through the lattice, rather than remaining innocent to the chemistry occurring at the surface.¹⁶

Received: April 4, 2022

Accepted: July 3, 2022

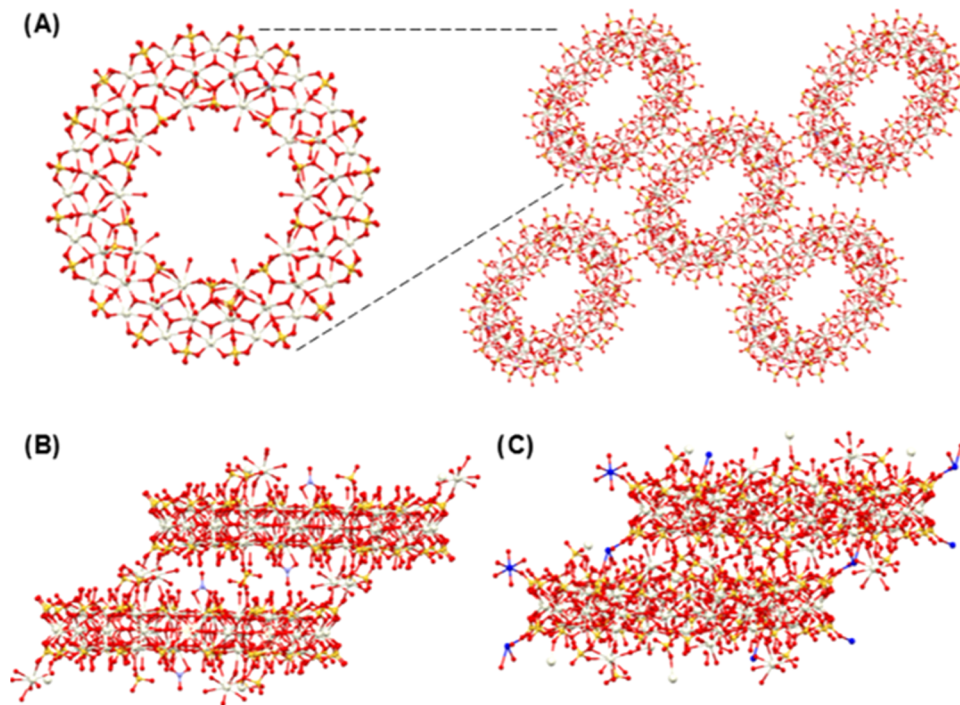


Figure 1. (A) CeCe₇₀ assembly with the enlarged repeated unit. (B) Interfacial linkage sites between two connected CeCe₇₀ rings. (C) Linkage sites between two connected CuCe₇₀ sites. Color scheme: light yellow, Ce; red, O; golden yellow, S; light blue, N; and royal blue, Cu. H atoms are omitted for clarity.

The reducibility of Ce⁴⁺ is greatly affected by and can be readily tuned through its local environment¹⁷ and geometry.¹⁸ Thus, ceria-based catalysts and catalyst supports have become indispensable within heterogeneous catalysis.¹⁹ Inspired by their ubiquity, a library of Ce-oxo clusters has been reported in recent years, often focusing on the synthesis to control the size and/or surface accessibility.^{20–24} Most recently, the Christou group modified a solvent used to facilitate the growth of intermediate Ce species to access a Ce₁₀₀-based oxo cluster, the highest nuclearity Ce-oxo cluster reported to date.²⁵

Additionally, work from the Nyman group expanded the metal oxysulfate torous motif, first reported in U and Zr,^{26,27} to Ce while providing insights to their assembly.^{28,29} In these crystallographically defined systems, every Ce atom is exposed to the surface in a donut-like structure (Figure 1) with a range of monomeric metal linkage moieties interconnecting the clusters to form one dimensional (1D) channels. Recent work from the Farha and Nyman teams further expanded the series to include a Ce₇₀ torus structure interconnected by Ce monomers and examined the photocatalytic and radical scavenging character of these clusters.³⁰ To date, most discrete Ce-oxo species have been studied in photocatalytic settings, given that the monodentate alkyl or aromatic capping agents present in other reported Ce-oxo clusters limit their thermal stability.^{24,31} However, the limited reports of utilizing discrete Ce-oxo clusters for thermal-based catalysis starkly contrasts the substantial volume of studies investigating bulk ceria as a catalyst and/or catalyst support in applications such as CO oxidation or CO₂ hydrogenation.^{32,33} Thus, the Ce₇₀ torus family, which instead features capping sulfates, is more amenable to interrogate as catalysts for more thermally demanding conditions. The unique surface architecture prompted us to further explore the efficacy of these clusters within gas-phase oxidation reactions.

In this study, we report the oxidation of CO over a range of MCe₇₀ oxysulfate clusters differing in the linkage cation between the clusters (M = Ce^{3+/4+}, Cd²⁺, Co²⁺, Cu²⁺, Fe^{2+/3+}, Ni²⁺, Zn²⁺). We demonstrate that the identity of this interfacial unit can alter the catalytic activity of the MCe₇₀ cluster family. The higher catalytic activity of CuCe₇₀ was corroborated with enhanced reducibility as observed through TPR-MS and *in situ* diffuse reflectance infrared Fourier transform spectroscopy (DRIFTS) studies. Furthermore, DRIFTS and CO isothermal physisorption measurements suggested stronger CO binding and enhanced CO uptake, respectively, by CuCe₇₀. Following the experimental observation of oxygen vacancy defects through Raman spectroscopy, density functional theory (DFT) calculations indicated that oxygen vacancy defect formation energetics differ among the bridging chain sites, with Cu interfacial sites exhibiting the lowest energy of formation, which further rationalizes its superior catalytic activity.

RESULTS AND DISCUSSION

The family of MCe₇₀ torus clusters (M = Ce^{3+/4+}, Cd²⁺, Co²⁺, Cu²⁺, Fe^{2+/3+}, Ni²⁺, and Zn²⁺) was synthesized according to published procedures.^{28,30} Notably, the MCe₇₀ clusters feature the shared formula of repeating Ce₇₀ toroids as previously reported through single-crystal X-ray diffraction (SC-XRD): [Ce₇₀(OH)₃₆(O)₆₄(SO₄)₆₀(H₂O)₁₀]⁴⁻ (see Table S1 for detailed formula listings).²⁸ The toroid clusters are linked through sulfate and monomeric cation-based interfacial units (Figure 1). Powder X-ray diffraction (PXRD) measurements of the clusters resulted in patterns consistent with prior reports and exhibited long-range order (Figure S1). Inductively coupled plasma-optical emission spectrometry (ICP-OES) demonstrated the successful incorporation of the linkage metal with a Ce:M ratio ranging from (6.1:1) to (7.6:1) in

addition to a consistent Ce:S ratio throughout all clusters (Table S2). The higher ratio of M in the powder samples as compared to the Ce:M ratio derived from SC-XRD (74:3) has been previously observed and documented. Interestingly, the lower concentration of M used to form MCe_{70} clusters increased the rate of assembly and M incorporation.²⁸ The synthetic procedures used to create microcrystalline MCe_{70} samples in this study used a smaller concentration of M as compared to the procedures previously reported to generate MCe_{70} single crystals.^{28–30} Nitrogen physisorption measurements were performed at 77 K to measure the apparent surface areas of all clusters (Figure S3), which are in agreement with previously reported surface areas of MCe_{70} clusters.³⁰

Following the characterization of the MCe_{70} cluster family, we explored the clusters' performance in CO oxidation in a packed bed reactor across a selected temperature regime (Figures S5–S11). Additionally, we investigated CeO_2 (commercially obtained) to contextualize the conversions of the MCe_{70} materials (Figure S12). CeO_2 achieved a 2.5% conversion at 200 °C, which is in the same range of most of the studied MCe_{70} catalysts and ~2-fold lower than CuCe_{70} before increasing to as high as 36% at 300 °C. All MCe_{70} catalysts were stable up to 200 °C, so the discussion is restricted to these temperatures. Conversion profiles at 200 °C indicated comparable conversions among all of the clusters, except the CuCe_{70} cluster, which exhibited a 3-fold higher conversion than CeCe_{70} and nearly 2-fold higher than that of the other MCe_{70} clusters (Figure 2). Postcatalysis PXRD patterns

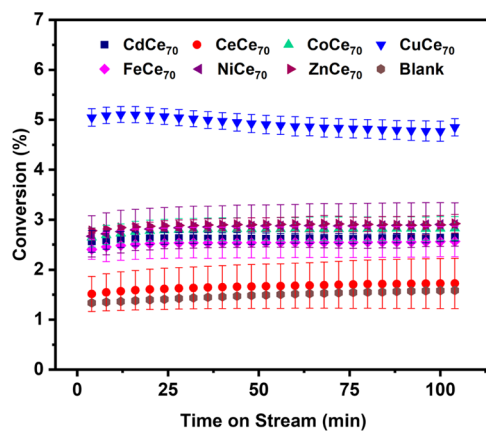


Figure 2. CO oxidation profiles at 200 °C of MCe_{70} clusters averaged over three trials. See Section 2 of the supporting information for the experimental details.

demonstrated retention in crystallinity without detectable formation of CeO_2 (Figure S2). Thus, we determined that the family of the clusters remained intact, and there is a difference in catalyst reactivity with $(\text{CuCe}_{70}) > (\text{CdCe}_{70}, \text{CoCe}_{70}, \text{FeCe}_{70}, \text{NiCe}_{70}, \text{ZnCe}_{70}) > (\text{CeCe}_{70})$. Moving forward, we elected to focus on CuCe_{70} and CeCe_{70} to interrogate the effect of linkage cation on the catalytic activity.

Next, we investigated the conversion profiles of CeCe_{70} and CuCe_{70} at 200 °C for 16 h on stream (Figure S13) to probe the catalyst stability. In these studies, CeCe_{70} exhibited constant reactivity, suggesting that it does not undergo an initial inductive effect that could have resulted in a lower conversion than CuCe_{70} . CuCe_{70} suffered a loss of ~20% catalytic activity after 3 h but remained constantly higher than CeCe_{70} . Moreover, through X-ray photoelectron spectroscopy

(XPS), we determined that CeCe_{70} and CuCe_{70} both contained similar amounts of Ce^{3+} (45%) post catalysis (Figures S16 and S17). From Auger electron spectroscopy (Figure S19), we determined that the Cu oxidation state of CuCe_{70} post catalysis was primarily Cu^{2+} with some population of Cu^{1+} sites; the CuCe_{70} Cu 2p kinetic energy of 919 eV was closer in value to that of CuO (920.2 eV) than that of Cu_2O (916.9 eV).

We further explored the effect of Cu as a linkage element, hypothesizing that the $\text{Cu}^{2+/1+}$ redox couple affects the overall reducibility of our catalysts given the literature precedence that the Cu^{2+} to Cu^{1+} redox couple served as a potent redox promoter on CeO_2 -based catalysts.³⁴ We investigated the temperature-programmed reduction (TPR) of the CeCe_{70} and CuCe_{70} catalysts under 5% CO/He while connected to a mass spectrometer (MS). We monitored the formation of detected CO_2 and SO_2 to distinguish between the reduction of Ce^{4+} to Ce^{3+} , a process that must be coupled with the oxidation of CO to CO_2 , as well as the reduction of surface sulfates on the clusters to SO_2 . For CeCe_{70} , we observed thermal conductivity detector (TCD) signals centered at 322 and 498 °C, whereas CuCe_{70} exhibited TCD signals at lower temperatures of 288 and 480 °C (Figure 3A,B). We therefore determined that CuCe_{70} is more reducible at lower temperatures. Within this temperature regime, TPR-MS traces demonstrated $[\text{CO}_2] \gg [\text{SO}_2]$ for the two sets of lower temperature peaks for both catalysts (Figure 3A,B). However, the low conversion of CO to CO_2 in the TPR-MS precludes definite conclusions about the

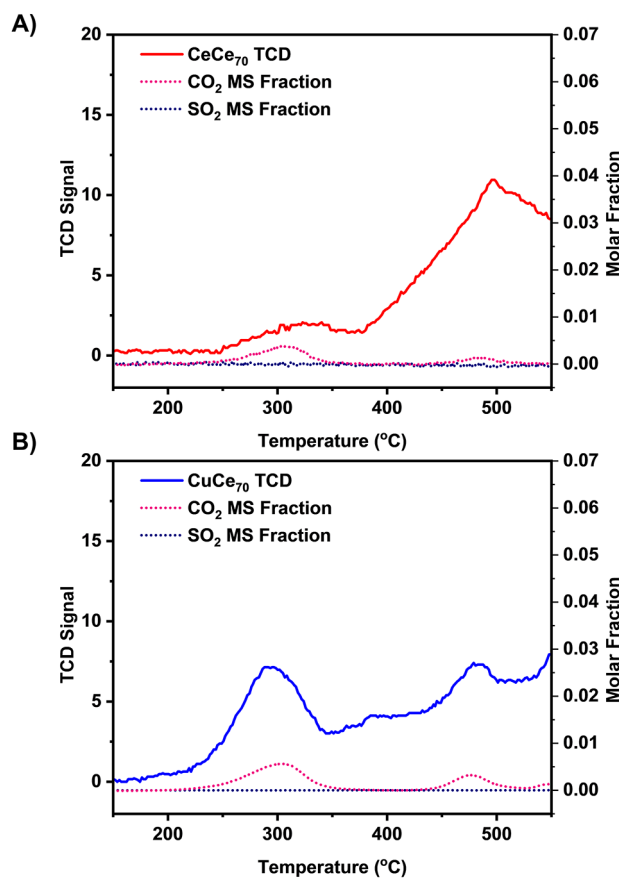


Figure 3. TPR-MS profiles of (A) CeCe_{70} and (B) CuCe_{70} under CO within 150–550 °C range. Remaining molar fraction corresponds to He, the carrier gas for the experiments.

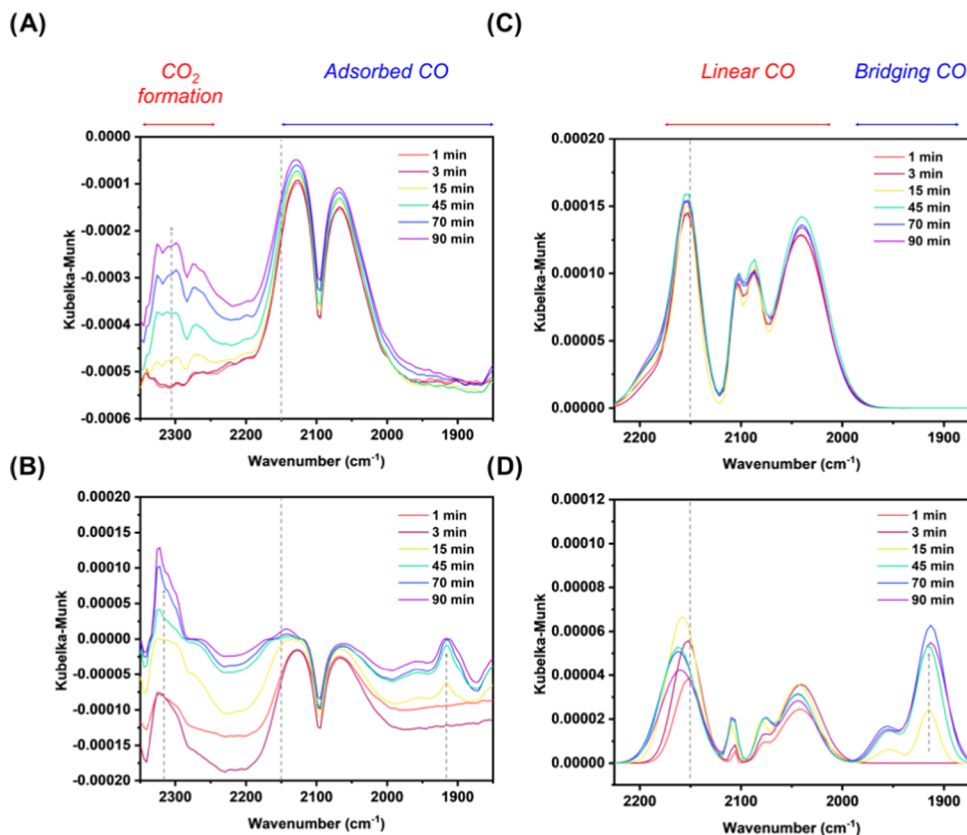


Figure 4. ^{13}CO DRIFTS data of (A) CeCe₇₀ and (B) CuCe₇₀ in the selected region collected at 200 °C. Time in legend corresponds to the duration of DRIFTS cell exposure to $^{13}\text{CO}/^{18}\text{O}_2$. Residual DRIFTS data shown in (C) of CeCe₇₀ and (D) of CuCe₇₀. Gray dotted lines were added to aid the visualization of 2150 cm^{-1} , while gray dotted arrows demonstrate the evolution of bridging CO peaks at the evolution of CO₂.

reducibility of specifically Ce⁴⁺ within this particular experiment; only 1.1 and 1.8 μmol of CO₂ were generated in CeCe₇₀ and CuCe₇₀, respectively, in the 290–350 °C range, corresponding to less than 1% of total moles of Ce reduced. The third TPR peak that appears ~650 °C in both catalysts features an equivalent production of CO₂ and SO₂, which complicates any conclusions that can be made about Ce⁴⁺ reduction at this temperature regime (Figure S20). Nonetheless, the TPR-MS data of the lower temperature TPD signals suggests that the identity of the cation in the bridging unit affects reduction within MCe₇₀ clusters.

We conducted CO/O₂ TPR experiments in which both CO and O₂ (in ~1:8 ratio) were flowed over CeCe₇₀ and CuCe₇₀ across a temperature range of 40–400 °C to gauge the catalysts' abilities to oxidize CO and form CO₂ (Figure S21). Under these conditions, CuCe₇₀ achieved a 50% conversion of CO at ~350 °C while CeCe₇₀ only achieved up to a 25% conversion of CO at 400 °C, indicating the improved oxidative activity of CuCe₇₀ as suggested by its earlier reduction in CO only TPR. Furthermore, the more reducible nature of CuCe₇₀ at lower temperatures coincides with its higher activity in the CO oxidation experiments as compared to CeCe₇₀. We were motivated to further investigate the evolution of Ce³⁺ within CeCe₇₀ and CuCe₇₀ to elucidate the effect of the linking cation on the reduction of Ce⁴⁺.

An available tool to study Ce³⁺ formation in CeO₂-based catalysts is monitoring the spin-orbit transition peak of Ce³⁺ appearing ~2150 cm^{-1} ^{35,36} as demonstrated by Wu et al.³⁷ Thus, we conducted *in situ* DRIFTS measurements of recirculated ^{13}CO in the presence of an $^{18}\text{O}_2$ rich atmosphere

flowed over CeCe₇₀ and CuCe₇₀. See Section 2 of the Supporting Information for more experimental details. Labeled ^{13}CO was used to further separate the spectrum of the reagent gas from the 2150 cm^{-1} region of interest.³⁸ We intentionally collected spectra with a resolution lower than that of the rotational coupling constants of CO (2 cm^{-1}) to remove the vibrational–rotational peaks of gas-phase CO to enable more facile data fitting.³⁹ As shown in Figure 4b, we detected a more noticeable shoulder around 2150 cm^{-1} in the DRIFTS of CuCe₇₀, suggesting a greater evolution of Ce³⁺ in CuCe₇₀ as compared to CeCe₇₀ (Figure 4a). Both catalysts demonstrated the formation of CO₂ with peaks appearing between 2250 and 2320 cm^{-1} . Interestingly, a strong peak at around 1915 cm^{-1} and a broader peak around 1955 cm^{-1} appeared during the DRIFTS experiment in CuCe₇₀ and not in CeCe₇₀.

To identify the contributions of the Ce³⁺ peak at 2150 cm^{-1} and explore the unexpected features between 1915 and 1955 cm^{-1} , we removed the gas-phase ^{13}CO signal and deconvoluted the resulting residual spectra between 1875 and 2225 cm^{-1} . Details of background treatment and the deconvolution procedure are located in the Supporting Information (Section 10). The residual peaks of CeCe₇₀ and CuCe₇₀ are plotted in Figure 4c,d. Peaks assigned to adsorbed CO were observed at 2040, 2078–2088, and 2105 cm^{-1} . In the CuCe₇₀ system, the second peak appeared slightly red-shifted to 2078 cm^{-1} , indicating a weaker C–O bond and suggesting a stronger CO interaction as compared to the peak centered around 2088 cm^{-1} in CeCe₇₀. Importantly, with the data deconvolution, we determined the amplitude of the Ce³⁺ peak at 2150 cm^{-1} (Tables S3 and S4). To follow the rate of

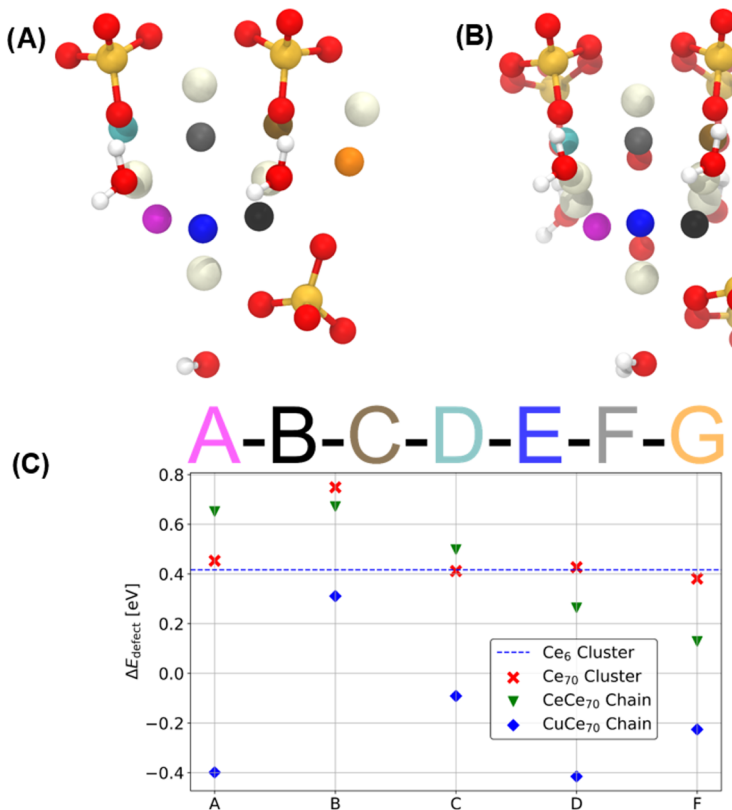


Figure 5. (A) Visualization and (B) alternate perspective of the $[\text{Ce}_7\text{O}_{10}(\text{SO}_4)_6(\text{H}_2\text{O})_5]^{4-}$ fragment used for constructing initial configurations. Atoms colored by element: light yellow, Ce; white, H; yellow, S; and red, O. The seven unique oxygens for hydrogen placement possibilities are color coded following the naming scheme below Figure 5A,B. (C) Calculated single oxygen vacancy formation energies (ΔE_{defect}) in the Ce₇₀ cluster (red crosses), the CeCe₇₀ chain (green triangles), and the CuCe₇₀ chain (blue diamonds). The calculated defect formation energy in an isolated Ce₆O₈(O₂CH)₈ cluster is plotted as a blue dashed line.

formation of Ce³⁺ in each catalyst, we normalized the 2150 cm^{-1} peak to the adsorbed CO peak at 2040 cm^{-1} (Figure S36). With these data, we concluded that there is a faster rate of Ce³⁺ formation and likely neighboring oxygen vacancy formation in CuCe₇₀ despite the ~5% fitting error associated with fits and surface site fluctuations too fast to appear on this time scale. This more facile Ce³⁺ formation aligns with the higher catalytic activity of CuCe₇₀ in CO oxidation.

Additionally, from the deconvolution of the CuCe₇₀ spectra, we observed a clear increase in the intensity of the lower frequency peaks (1915 and 1955 cm^{-1}), while the 2040 and 2150 cm^{-1} peaks proportionally decreased. We reasoned that the Cu must be contributing to this interaction given the absence of these low-frequency peaks in CeCe₇₀. We determined that the lower frequency peaks are unlikely to result from CO linearly bonding solely to Cu species, as prior reports indicate shifts $>2055 \text{ cm}^{-1}$ for $\text{Cu}^{x+}-^{13}\text{CO}$ species ($>2100 \text{ cm}^{-1}$ correlates to $\text{Cu}^{x+}-^{12}\text{CO}$ species).⁴⁰ Since this region is where bridging CO stretches are expected,⁴¹ the peaks assigned at 1915 and 1955 cm^{-1} can likely be attributed to (1) bridging CO forming a Cu–CO–Ce dimer and/or (2) bridging CO forming a Ce–CO–Ce dimer that is facilitated by nearby Cu. The ability to form bridging CO in CuCe₇₀ as opposed to CeCe₇₀ implied a higher CO uptake in CuCe₇₀ given this bridging motif is more energetically challenging to access at lower CO concentrations, as previously reported through Monte Carlo simulations.⁴² To further explore this hypothesis, we conducted CO isothermal adsorption measurements at 87 K, and we observed an almost 2-fold increase in

CO uptake by CuCe₇₀ as compared to CeCe₇₀, consistent with its higher N₂ uptake (Figure S37). The higher CO uptake, which likely enables the unique bridging CO stretches observed in the CuCe₇₀ DRIFTS spectra, is consistent with the observed superior reactivity of CuCe₇₀.

After detecting the evolution of Ce³⁺ in our DRIFTS data, we further explored the formation of neighboring O vacancies, species known to directly participate in oxidative or reduction processes,^{13,15} using Raman spectroscopy. Measurements under ambient conditions indicated that vacancies are present in the pristine CeCe₇₀ and CuCe₇₀ clusters, in agreement with prior studies by Wang et al. (Figure S38).³⁰ Both catalysts demonstrated a signal around 400 cm^{-1} that is attributed to surface Ce–O vibrations with a larger intensity than the peak around 465 cm^{-1} associated with bulk Ce–O vibrations.⁴³ Herman and co-workers previously demonstrated that a shoulder in Raman spectra of ceria nanoparticles as small as 6 nm at $\sim 400 \text{ cm}^{-1}$ is due to combined effects of strain and photon confinement.⁴⁴ However, more intense surface than bulk features is highly unusual, even among CeO₂ nanoparticles, further highlighting their cluster-like nature as opposed to a nanostructured solid-state character. The intensities found between 500 and 700 cm^{-1} indicate a rich defect character for both clusters.⁴⁵ Given that both clusters are able to accommodate oxygen defects, we conjectured that the ability to form the defects in the Ce₇₀ toroid system could be affected by the linkage element present.

To further investigate the formation of oxygen vacancy defects within CeCe₇₀ and CuCe₇₀, we calculated and

compared the defect formation energy in these systems using density functional theory. Based on previously published structural data of Colliard et al. and Wang et al., we first manually created an idealized cluster model of a Ce₇₀ toroid with D_{10h} symmetry.^{28–30} Due to the missing/disordered hydrogen atoms in the experimental structure solutions, we rigorously tested all reasonable hydrogen placements adhering to the D_{10h} symmetry. See Section 13 in the Supporting Information for a detailed discussion of possible hydrogen placements. The resulting 22 hydrogen patterns were optimized at the Perdew–Burke–Ernzerhof (PBE) level of theory and the resulting relative energies were compared. We found two hydrogen placements within a range of 9 kJ/mol of each other, while all other placements are found to be more than 450 kJ/mol higher in energy. We therefore chose the hydrogen placement with the lowest energy for our further investigations. The second-lowest energy configuration can also be expected to occur, in line with –O/OH disorder observed in the bond valence sum calculations of Colliard et al.²⁸ A comparison of all hydrogen placements and their relative energies is given in Section 13 of the Supporting Information.

Using the selected hydrogen placement scheme, we investigated the formation energy (ΔE_{defect}) for a defect consisting of a single missing neutral oxygen atom using the formula $\Delta E_{\text{defect}} = E(\text{toroid w. defect}) + E\left(\frac{1}{2}\text{O}_2\right) - E(\text{toroid})$. The selected hydrogen placement scheme allows for five distinct neutral oxygen vacancies. The resulting defective toroid was modeled in a triplet spin state, as the spin coupling between Ce atoms adjacent to the defect site is expected to be small and the accuracy of the calculation setups is expected to be lower than the possible effects observable by employing the broken symmetry approach to describe a singlet antiferromagnetic (AFM) spin state.⁴⁶ To validate the triplet state, we also calculated the defect formation energies using a singlet spin state of the defective cluster. Absolute energies of the clusters as well as defect formation energies are significantly lower in the triplet state, confirming our spin state choice. See Figure S43 for more details. We note here that the defect formation energies calculated using the singlet state of the defective cluster and bulk ceria are surprisingly close to some values reported in the literature where no spin state is specified.^{47–49} Our results underline the importance of investigating different spin states (and reporting what spin state was used) when modeling defective ceria using DFT. All calculated defect energies are given in Section 13 of the Supporting Information.

We calculated the defect formation energies of the five possible defect sites in the Ce₇₀ cluster (labeled A–D and F, see Figure 5A,B). The average value is 0.48 eV, with a minimum value of 0.38 eV and one outlier at 0.75 eV (Figure 5C). For comparison, we also calculated the bulk defect energies of bulk CeO₂ and a Ce₆O₈(O₂CH)₈ cluster (an often-used precursor in Ce-oxo cluster synthesis²⁰ or building block in metal–organic frameworks⁵⁰ and comparable to the Ce₆ octahedron unit in the toroid) using the same methodology to be 2.32 and 0.42 eV, respectively (computational details are given in Section 13 of the Supporting Information). We therefore observe the same trend of decreasing ΔE_{defect} with decreasing particle size that is also observed experimentally.^{51,52} Our ΔE_{defect} of bulk ceria is slightly lower than previously reported values calculated using DFT+U (e.g., 3.2

eV by Chen et al. using $U_f = 6.2$ eV).⁵³ Ziemba et al. calculated ΔE_{defect} for ceria surfaces using DFT+U ($U_f = 4.5$ eV) to be in the range of 1.1–2.1 eV.^{54,55} This clearly shows the overall trend of a decreasing ΔE_{defect} for a decreasing dimensionality and extension of the ceria particles and agrees well with our results. Our Ce₇₀ cluster model furthermore exhibits no significant deviation in ΔE_{defect} from the isolated Ce₆O₈(O₂CH)₈ cluster even though it is an extended system.

To investigate the influence of the bridging Ce and Cu units in the experiment, we extended our model into a one-dimensional chain by adding the bridging CeO₄ or CuO₄ unit from the single crystal-derived structure solution to the DFT+U optimized cluster and applying one-dimensional periodic boundary conditions (1D PBC). In the case of Ce, two oxygens were saturated with two H atoms each. For the Cu bridge, two oxygens were saturated with two H atoms each, and the remaining two oxygens were saturated with one H atom each. After the relaxation of the unit cell length and subsequent geometry optimization, the same methodology as for the cluster model was applied to obtain ΔE_{defect} for the five possible defect sites (labeled A–D and F, see Figure 5A,B). The resulting defect formation energies of the Ce-bridged chain (Figure 5C) are in good agreement with the Ce₇₀ cluster model values. The average ΔE_{defect} is 0.44 eV for the CeCe₇₀ chain, while the spread is significantly larger than in the Ce₇₀ cluster model (minimum of 0.13 eV and maximum of 0.67 eV). Figure 5C compares all three model systems and the Ce₆ cluster. More details and a comparison of the effect of varying U_d values on the resulting defect formation energies in the Cu-bridged chains are given in Section 13 of the Supporting Information.

From Figure 5C, it is clearly visible that the substitution of Ce with Cu in the bridging unit results in a significant decrease of ΔE_{defect} . This conclusion agrees well with the experimental observation of increased activity for the Cu system but is still surprising. The chemical nature of the system would, in our opinion, suggest a highly localized nature of the defect formations. The Ce₇₀ cluster model also suggests a highly localized electron redistribution upon formation of the oxygen vacancy, with the two free electrons localizing in the Ce f orbitals of two adjacent Ce atoms. In the case of the Ce-bridged periodic model, we also observe no significant charge transfer upon formation of the oxygen vacancy beyond the two adjacent Ce atoms. In the Cu-bridged chain, however, a significant charge transfer toward the Cu atom in the bridge is observed (decrease of Mulliken charge on Cu from 0.47 to 0.18). The previous doublet spin state on Cu transforms into a singlet state in our calculations, suggesting a reduction of the Cu. The defective system, however, still favors the anticipated quartet state and the three unpaired electrons localize on the three Ce atoms adjacent to the oxygen vacancy. This charge transfer is unexpected, and we are at this stage unable to determine whether this is an artifact of the level of theory applied here or if this is indeed close to the true electronic ground state of the system. Further computational and experimental investigations are needed to better model the effects of the bridge on the nearby defect sites. Nonetheless, we are hopeful that our initial systematic study into modeling defect energetics within experimentally derived Ce-oxo clusters will motivate future investigations among other cluster shapes and compositions given the rarity of such inquiries.

While Cu/CeO₂-based catalysts have been well-studied for CO oxidation, they often are in the form of polydisperse

oxides, hindering the understanding of the real active sites.⁵⁶ Our inquiry into highly crystalline, discrete clusters provides an alternative approach to derive meaningful insights relating to structure and reactivity with increased confidence of the atomic-level structure. Our results indicated that even a single ion-based linkage unit between neighboring clusters can serve as an active interface that readily tunes the reducibility and defect formation energetics of the Ce₇₀ ring and consequently the catalytic activity. We envision that our study can further motivate the creation of single/few ion⁵⁷ or ultrathin⁵⁸ interfaces within ceria-containing nanostructures.

CONCLUSIONS

In summary, we have established a correlation between higher catalytic activity for CO oxidation and the identity of the bridging cationic units linking the Ce₇₀ toroids within the MCe₇₀ cluster assemblies. We observed the highest CO conversion with CuCe₇₀, containing Cu in the bridging units. Through CO-TPR studies, we observed that CuCe₇₀ is more reducible than CeCe₇₀. *In situ* DRIFTS data suggested a faster formation of Ce³⁺ and identified unique CO bridging adsorption bands within CuCe₇₀, while CO isotherms confirmed higher CO uptake in CuCe₇₀ as compared to CeCe₇₀. Lastly, calculations determined that the presence of Cu in the bridging unit can substantially lower the energetic requirements to form a single oxygen vacancy in CuCe₇₀ compared to CeCe₇₀. Thus, we conclude that the incorporation of Cu in the bridging chain of the Ce₇₀ torus family results in superior catalytic activity for CO oxidation due to its higher reducibility, enhanced CO binding and uptake, and more favorable oxygen vacancy defect formation. This investigation into gas-phase reactivity and cluster chemistry demonstrates that subtle atomic changes can affect the assemblies' properties. We are hopeful that this study will inspire further inquiry into this fascinating array of species as well as the expansion of further metal-oxo clusters or bulk metal oxide architectures with unique interfaces.

EXPERIMENTAL SECTION

MCe₇₀ Syntheses. CeCe₇₀, CoCe₇₀, CuCe₇₀, FeCe₇₀, and NiCe₇₀ were synthesized according to published procedures for microcrystalline samples.³⁰ CdCe₇₀ was synthesized according to published procedure for CdCe₇₀—standard, yet was left to sit undisturbed for 5 days.²⁸ ZnCe₇₀ was synthesized according to modifications from published procedure and is detailed below.²⁸

87 mg of Zn(NO₃)₂ and 110 mg of Ce(SO₄)₂ were placed in 2 mL of water with 20 μL of a 1.0 M aqueous solution of tetrabutylammonium chloride. The clusters were left for 36 h undisturbed at room temperature.

After synthesis, all clusters underwent the following washing procedure:

The as-synthesized cluster solutions were centrifuged to decant the collected solid from the mother solution. The isolated cluster was then washed twice more with deionised (DI) water, followed by centrifugation, and then twice with ethanol. After the second ethanol wash and centrifugation, the isolated powder dried overnight on the benchtop.

Catalyst Reactivity Studies. In a typical experiment, ~40 mg of catalyst (based on ~0.3 mmol of Ce₇₀) was diluted with 1 g of quartz sand (trace-metal grade) and packed in a quartz tube plugged with quartz wool. The height of the bed was approximately 1 in. The sample was pretreated at 200 °C for 2 h with a flow rate of 20 sccm of 20% O₂/He. After pretreatment, the catalyst was immediately exposed to reactant gases of 20 sccm of 0.5% CO/20% O₂/He and 20 sccm of 20% O₂/He co-fed with 50 sccm of N₂. For a typical temperature

ramp-up and ramp-down profile, the reactor was first cooled to 150 °C at a rate of 10 °C/min and held for 2 h, then ramped to 200 °C at a ramp rate of 10 °C/min and held for 2 h, then ramped to 250 °C at a ramp rate of 10 °C/min and held for 2 h, then ramped to 300 °C at a ramp rate of 10 °C/min and held for 4 h, then cooled to 250 °C at a rate of 10 °C/min and held for 2 h, then cooled to 200 °C at a rate of 10 °C/min and held for 2 h, and then cooled to 150 °C at a rate of 10 °C/min and held for 2 h before a final cool down to 40 °C. To generate the 200 °C conversion data to gather triplicate data points (Figure 1 in MS), a typical experiment repeated the pretreatment protocol of heating the reactor tube at 200 °C for 2 h with a flow rate of 20 sccm of 20% O₂/He. To remain consistent with the prior temperature ramp profile described above, the catalyst was first cooled to 150 °C and held for 2 h under the reactant conditions described above before ramping to 200 °C at 10 °C/min and held for 2 h to generate the additional trials used for catalyst comparisons. For the stability studies of CeCe₇₀ and CuCe₇₀, each catalyst was again pretreated at 200 °C for 2 h with a flow rate of 20 sccm of 20% O₂/He. Then, the catalyst was heated at 200 °C for over 16 h under the reactant conditions mentioned above to remain consistent with the other studies.

CO Temperature-Programmed Reduction Experiments. CO TPR. Approximately 70 mg of material was placed in a quartz reaction tube plugged between quartz wool and quartz sand. Temperature-programmed experiments were performed on an Altamira AMI-200 instrument equipped with a thermal conductivity detector (TCD). In a typical experiment, catalysts were pretreated at 200 °C for 2 h under 30 cc/min under 10% O₂/He and then cooled to 40 °C in 30 sccm He. Then, the system was heated to 900 °C at a ramp rate of 10 °C/min under 25 sccm of 5% CO/He with a carrier gas flow of 5 cc/min of He. Then, the system was cooled to 40 °C at a ramp rate of 30 °C/min under 30 cc/min of N₂.

CO/O₂ TPR. Approximately 30 mg of material was placed in a quartz reaction tube mixed with white quartz sand (Aldrich) to a height of 1 cm and plugged between layers of quartz wool and quartz sand. Temperature-programmed reaction experiments were performed on an Altamira AMI-200 instrument equipped with an in-line atmospheric mass spectrometer (an SRS RGA100 quadrupole mass spectrometer with a custom-built sampling manifold). In a typical experiment, the sample was reduced in 10% H₂/N₂ (Airgas, certified) at 200 °C for 2 h prior to the CO/O₂ TPR. The sample was then cooled down to 40 °C under He (Airgas, UHP) flowing at 30 sccm and finally heated to 400 °C at a ramp rate of 10 °C/min under 10 sccm of 5% CO/He (Airgas, certified) and 40 sccm of 10% O₂/He (Airgas, certified). Ionic masses, *m/z*, of 28 (CO), 44 (CO₂), 32 (O₂), and 4 (He) were continuously monitored *via* atmospheric mass spectrometer. Molar fractions given in the plots were corrected for ionic sensitivities and fragmentation patterns and all normalized including He (not shown).

In Situ DRIFTS Measurements. *In situ* ¹³CO DRIFTS measurements were carried out using a Nicolet iS50 Fourier-transform infrared (FTIR) spectrometer equipped with a Harrick Scientific Praying Mantis DRIFTS accessory and a high-temperature reaction chamber. Each sample (12 mg of each) was crushed using a mortar and pestle and placed in the sample cup of the DRIFT reaction chamber on top of a bed of KBr. The temperature was raised to 200 °C under 10% O₂/Ar (Airgas, UHP grade) flowing at 50 sccm. A background spectrum was collected after 200 °C for 2 h and used as a reference for the subsequent spectra. Then, a gaseous mixture of ¹³CO (20.0 mbar) and ¹⁸O₂ (50 mbar) in He (1000 mbar) was recirculated through a custom-built system equilibrated at 1070 mbar. Infrared (IR) spectra were acquired over the course of ~2 h until spectral changes in the CO and CO₂ stretch region (~2200–1900 cm⁻¹) were negligible. The spectra resolution was 4 cm⁻¹. The system was evacuated under Ar as the reaction chamber cooled back down.

ASSOCIATED CONTENT

Supporting Information

The Supporting Information is available free of charge at <https://pubs.acs.org/doi/10.1021/acsami.2c05937>.

PXRD patterns; isothermal adsorption data; reactivity data; XPS data/fits; TPR-MS data; DRIFTS spectra/fits; Raman spectra; and simulation details ([PDF](#))

AUTHOR INFORMATION

Corresponding Author

Omar K. Farha – International Institute for Nanotechnology and Department of Chemistry, Northwestern University, Evanston, Illinois 60208, United States; Department of Chemical and Biological Engineering, Northwestern University, Evanston, Illinois 60208, United States; orcid.org/0000-0002-9904-9845; Email: o-farha@northwestern.edu

Authors

Megan C. Wasson – International Institute for Nanotechnology and Department of Chemistry, Northwestern University, Evanston, Illinois 60208, United States; orcid.org/0000-0002-9384-2033

Xingjie Wang – International Institute for Nanotechnology and Department of Chemistry, Northwestern University, Evanston, Illinois 60208, United States; orcid.org/0000-0002-5802-9944

Patrick Melix – Department of Chemical and Biological Engineering, Northwestern University, Evanston, Illinois 60208, United States; Wilhelm-Ostwald-Institut für Physikalische und Theoretische Chemie, Universität Leipzig, 04103 Leipzig, Germany; orcid.org/0000-0002-1027-1272

Selim Alayoglu – Reactor Engineering and Catalyst Testing Core, Northwestern University, Evanston, Illinois 60208, United States

Andrew T. Y. Wolek – Department of Chemical and Biological Engineering, Northwestern University, Evanston, Illinois 60208, United States

Ian Colliard – Department of Chemistry, Oregon State University, Corvallis, Oregon 97331, United States; orcid.org/0000-0003-1883-1155

Florencia A. Son – International Institute for Nanotechnology and Department of Chemistry, Northwestern University, Evanston, Illinois 60208, United States; orcid.org/0000-0002-7524-3774

Haomiao Xie – International Institute for Nanotechnology and Department of Chemistry, Northwestern University, Evanston, Illinois 60208, United States; orcid.org/0000-0001-7688-6571

Eric Weitz – International Institute for Nanotechnology and Department of Chemistry, Northwestern University, Evanston, Illinois 60208, United States; orcid.org/0000-0002-7447-4060

Timur Islamoglu – International Institute for Nanotechnology and Department of Chemistry, Northwestern University, Evanston, Illinois 60208, United States; orcid.org/0000-0003-3688-9158

May Nyman – Department of Chemistry, Oregon State University, Corvallis, Oregon 97331, United States; orcid.org/0000-0002-1787-0518

Randall Q. Snurr – Department of Chemical and Biological Engineering, Northwestern University, Evanston, Illinois 60208, United States; orcid.org/0000-0003-2925-9246

Justin M. Notestein – Department of Chemical and Biological Engineering, Northwestern University, Evanston, Illinois 60208, United States; orcid.org/0000-0003-1780-7356

Complete contact information is available at: <https://pubs.acs.org/10.1021/acsami.2c05937>

Author Contributions

All authors have given approval to the final version of the manuscript. M.C.W. and X.W. contributed equally to this work.

Notes

The authors declare no competing financial interest.

ACKNOWLEDGMENTS

The authors gratefully acknowledge the Northwestern University Institute for Catalysis in Energy Processes (ICEP), funded by the DOE, Office of Basic Energy Sciences (award number DE-FG02-03ER15457). M.C.W. is supported by the NSF Graduate Research Fellowship under grant DGE-1842165. P.M. acknowledges funding by the Humboldt Foundation through a Feodor Lynen fellowship. A.T.Y.W. is supported by the National Science Foundation under Cooperative Agreement No. EEC-1647722. F.A.S. is supported by a fellowship award through the National Defense Science and Engineering Graduate (NDSEG) Fellowship Program and a Ryan Fellowship through the International Institute for Nanotechnology at Northwestern University. I.C. and M.N. acknowledge funding from the Department of Energy, National Nuclear Security Administration (NNSA) under Award Number DE-NA0003763. The REACT Facility of the Northwestern University Center for Catalysis and Surface Science is supported by a grant from the DOE (DE-SC0001329). This work made use of the IMSERC X-ray facility at Northwestern University, which has received support from the Soft and Hybrid Nanotechnology Experimental (SHyNE) Resource (NSF ECCS-1542205), the State of Illinois, and the International Institute for Nanotechnology (IIN). Also, this work made use of the Keck-II facility of Northwestern University's NUANCE Center, which has received support from the Soft and Hybrid Nanotechnology Experimental (SHyNE) Resource (NSF ECCS-1542205); the MRSEC program (NSF DMR-1720139) at the Materials Research Center; the International Institute for Nanotechnology (IIN); the Keck Foundation; and the State of Illinois, through the IIN. This research was supported in part through the computational resources and staff contributions provided for the Quest high-performance computing facility at Northwestern University, which is jointly supported by the Office of the Provost, the Office for Research, and Northwestern University Information Technology. This research used resources of the National Energy Research Scientific Computing Center (NERSC), a Department of Energy Office of Science User Facility located at Lawrence Berkeley National Laboratory, operated under Contract No. DE-AC02-05CH11231 using NERSC award BES-ERCAP0018367.

■ REFERENCES

- (1) Liu, L.; Corma, A. Metal Catalysts for Heterogeneous Catalysis: From Single Atoms to Nanoclusters and Nanoparticles. *Chem. Rev.* **2018**, *118*, 4981–5079.
- (2) Jose, R.; Thavasi, V.; Ramakrishna, S. Metal Oxides for Dye-Sensitized Solar Cells. *J. Am. Ceram. Soc.* **2009**, *92*, 289–301.
- (3) Nikolova, M. P.; Chavali, M. S. Metal Oxide Nanoparticles as Biomedical Materials. *Biomimetics* **2020**, *5*, No. 27.
- (4) Somorjai, G. A.; Li, Y. Impact of Surface Chemistry. *Proc. Natl. Acad. Sci. U.S.A.* **2011**, *108*, 917–924.
- (5) Zhou, Z. Y.; Tian, N.; Li, J. T.; Broadwell, I.; Sun, S. G. Nanomaterials of High Surface Energy with Exceptional Properties in Catalysis and Energy Storage. *Chem. Soc. Rev.* **2011**, *40*, 4167–4185.
- (6) Tian, N.; Zhou, Z. Y.; Sun, S. G.; Ding, Y.; Zhong, L. W. Synthesis of Tetrahedral Platinum Nanocrystals with High-Index Facets and High Electro-Oxidation Activity. *Science* **2007**, *316*, 732–735.
- (7) Jana, N. R.; Chen, Y.; Peng, X. Size- and Shape-Controlled Magnetic (Cr, Mn, Fe, Co, Ni) Oxide Nanocrystals via a Simple and General Approach. *Chem. Mater.* **2004**, *16*, 3931–3935.
- (8) Jiao, K.; Zhang, B.; Yue, B.; Ren, Y.; Liu, S.; Yan, S.; Dickinson, C.; Zhou, W.; He, H. Growth of Porous Single-Crystal Cr₂O₃ in a 3-D Mesopore System. *Chem. Commun.* **2005**, *45*, 5618–5620.
- (9) Shi, Y.; Lee, S. C.; Monti, M.; Wang, C.; Feng, Z. A.; Nix, W. D.; Toney, M. F.; Sinclair, R.; Chueh, W. C. Growth of Highly Strained CeO₂ Ultrathin Films. *ACS Nano* **2016**, *10*, 9938–9947.
- (10) Wasson, M. C.; Buru, C. T.; Chen, Z.; Islamoglu, T.; Farha, O. K. Metal–Organic Frameworks: A Tunable Platform to Access Single-Site Heterogeneous Catalysts. *Appl. Catal., A* **2019**, *586*, No. 117214.
- (11) Jin, R.; Li, G.; Sharma, S.; Li, Y.; Du, X. Toward Active-Site Tailoring in Heterogeneous Catalysis by Atomically Precise Metal Nanoclusters with Crystallographic Structures. *Chem. Rev.* **2021**, *121*, 567–648.
- (12) Zhang, Y.; de Azambuja, F.; Parac-Vogt, T. N. The Forgotten Chemistry of Group(IV) Metals: A Survey on the Synthesis, Structure, and Properties of Discrete Zr(IV), Hf(IV), and Ti(IV) Oxo Clusters. *Coord. Chem. Rev.* **2021**, *438*, No. 213886.
- (13) Mullins, D. R. The Surface Chemistry of Cerium Oxide. *Surf. Sci. Rep.* **2015**, *70*, 42–85.
- (14) Paier, J.; Penschke, C.; Sauer, J. Oxygen Defects and Surface Chemistry of Ceria: Quantum Chemical Studies Compared to Experiment. *Chem. Rev.* **2013**, *113*, 3949–3985.
- (15) Nolan, M.; Parker, S. C.; Watson, G. W. The Electronic Structure of Oxygen Vacancy Defects at the Low Index Surfaces of Ceria. *Surf. Sci.* **2005**, *595*, 223–232.
- (16) Esch, F.; Fabris, S.; Zhou, L.; Montini, T.; Africh, C.; Fornasiero, P.; Comelli, G.; Rosei, R. Chemistry: Electron Localization Determines Defect Formation on Ceria Substrates. *Science* **2005**, *309*, 752–755.
- (17) Reidy, R. F.; Swider, K. E. Determination of the Cerium Oxidation State in Cerium Vanadate. *J. Am. Ceram. Soc.* **1995**, *78*, 1121–1122.
- (18) Stubenrauch, J.; Vohs, J. M. Interaction of CO with Rh Supported on Stoichiometric and Reduced CeO₂(111) and CeO₂(100) Surfaces. *J. Catal.* **1996**, *159*, 50–57.
- (19) Trovarelli, A. Catalytic Properties of Ceria and CeO₂-Containing Materials. *Catal. Rev.* **1996**, *38*, 439–520.
- (20) Estes, S. L.; Antonio, M. R.; Soderholm, L. Tetravalent Ce in the Nitrate-Decorated Hexanuclear Cluster [Ce₆(M₃-O)₄(M₃-OH)-₄]¹²⁺: A Structural End Point for Ceria Nanoparticles. *J. Phys. Chem. C* **2016**, *120*, 5810–5818.
- (21) Mathey, L.; Paul, M.; Copéret, C.; Tsurugi, H.; Mashima, K. Cerium(IV) Hexanuclear Clusters from Cerium(III) Precursors: Molecular Models for Oxidative Growth of Ceria Nanoparticles. *Chem. - Eur. J.* **2015**, *21*, 13454–13461.
- (22) Malaestean, I. L.; Ellern, A.; Baca, S.; Kögerler, P. Cerium Oxide Nanoclusters: Commensurate with Concepts of Polyoxometalate Chemistry? *Chem. Commun.* **2012**, *48*, 1499–1501.
- (23) Mitchell, K. J.; Abboud, K. A.; Christou, G. Atomically-Precise Colloidal Nanoparticles of Cerium Dioxide. *Nat. Commun.* **2017**, *8*, No. 1445.
- (24) Wasson, M. C.; Zhang, X.; Otake, K.-I.; Rosen, A. S.; Alayoglu, S.; Krzyaniak, M. D.; Chen, Z.; Redfern, L. R.; Robison, L.; Son, F. A.; Chen, Y.; Islamoglu, T.; Notestein, J. M.; Snurr, R. Q.; Wasielewski, M. R.; Farha, O. K. Supramolecular Porous Assemblies of Atomically Precise Catalytically Active Cerium-Based Clusters. *Chem. Mater.* **2020**, *32*, 8522–8529.
- (25) Russell-Webster, B.; Lopez-Nieto, J.; Abboud, K. A.; Christou, G. Truly Monodisperse Molecular Nanoparticles of Cerium Dioxide of 2.4 nm Dimensions: A {Ce100O167} Cluster. *Angew. Chem., Int. Ed.* **2021**, *60*, 12591–12596.
- (26) Colliard, I.; Morrison, G.; zur Loye, H. C.; Nyman, M. Supramolecular Assembly of U(IV) Clusters and Superatoms with Unconventional Counterions. *J. Am. Chem. Soc.* **2020**, *142*, 9039–9047.
- (27) Øien-Ødegaard, S.; Baziotti, C.; Redekop, E. A.; Prytz, Ø.; Lillerud, K. P.; Olsbye, U. A Toroidal Zr₇₀ Oxsulfate Cluster and Its Diverse Packing Structures. *Angew. Chem., Int. Ed.* **2020**, *59*, 21397–21402.
- (28) Colliard, I.; Nyman, M. CeIV₇₀ Oxsulfate Rings, Frameworks, Supramolecular Assembly, and Redox Activity. *Angew. Chem., Int. Ed.* **2021**, *60*, 7308–7315.
- (29) Colliard, I.; Brown, J. C.; Fast, D. B.; Sockwell, A. K.; Hixon, A. E.; Nyman, M. Snapshots of Ce₇₀Toroid Assembly from Solids and Solution. *J. Am. Chem. Soc.* **2021**, *143*, 9612–9621.
- (30) Wang, X.; Xie, H.; Knapp, J. G.; Wasson, M. C.; Wu, Y.; Ma, K.; Stone, A. E.B.; Krzyaniak, M. D.; Chen, Y.; Zhang, X.; Notestein, J. M.; Wasielewski, M. R.; Farha, O. K. Mechanistic Investigation of Enhanced Catalytic Selectivity toward Alcohol Oxidation with Ce-Oxsulfate Clusters. *J. Am. Chem. Soc.* **2022**, *144*, 12092–12101.
- (31) Shirase, S.; Tamaki, S.; Shinohara, K.; Hiroswa, K.; Tsurugi, H.; Satoh, T.; Mashima, K. Cerium(IV) Carboxylate Photocatalyst for Catalytic Radical Formation from Carboxylic Acids: Decarboxylative Oxygenation of Aliphatic Carboxylic Acids and Lactonization of Aromatic Carboxylic Acids. *J. Am. Chem. Soc.* **2020**, *142*, 5668–5675.
- (32) Zhou, K.; Wang, X.; Sun, X.; Peng, Q.; Li, Y. Enhanced Catalytic Activity of Ceria Nanorods from Well-Defined Reactive Crystal Planes. *J. Catal.* **2005**, *229*, 206–212.
- (33) Chang, K.; Zhang, H.; Cheng, M. J.; Lu, Q. Application of Ceria in CO₂ Conversion Catalysis. *ACS Catal.* **2020**, *10*, 613–631.
- (34) Kacimi, S.; Barbier, J.; Taha, R.; Duprez, D. Oxygen Storage Capacity of Promoted Rh/CeC₂ Catalysts. Exceptional Behavior of RhCu/CeO₂. *Catal. Lett.* **1993**, *22*, 343–350.
- (35) Binet, C.; Daturi, M.; Lavalle, J. C. IR Study of Polycrystalline Ceria Properties in Oxidised and Reduced States. *Catal. Today* **1999**, *50*, 207–225.
- (36) Binet, C.; Badri, A.; Lavalle, J. C. A Spectroscopic Characterization of the Reduction of Ceria from Electronic Transitions of Intrinsic Point Defects. *J. Phys. Chem. A* **1994**, *98*, 6392–6398.
- (37) Wu, W.; Savereide, L. M.; Notestein, J.; Weitz, E. In-Situ IR Spectroscopy as a Probe of Oxidation/Reduction of Ce in Nanostructured CeO₂. *Appl. Surf. Sci.* **2018**, *445*, 548–554.
- (38) Luo, L.; Hua, Q.; Jiang, Z.; Huang, W. A Pulse Chemisorption/Reaction System for in Situ and Time-Resolved DRIFTS Studies of Catalytic Reactions on Solid Surfaces. *Rev. Sci. Instrum.* **2014**, *85*, No. 064103.
- (39) Mina-Camilde, N.; Manzanares, I.C.; Caballero, J. F. Molecular Constants of Carbon Monoxide at v = 0, 1, 2, and 3: A Vibrational Spectroscopy Experiment in Physical Chemistry. *J. Chem. Educ.* **1996**, *73*, 804–807.
- (40) Hadjiivanov, K.; Knözinger, H. FTIR Study of CO and NO Adsorption and Coadsorption on a Cu/SiO₂ Catalyst: Probing the Oxidation State of Copper. *Phys. Chem. Chem. Phys.* **2001**, *3*, 1132–1137.
- (41) Aubke, F.; Wang, C. Carbon Monoxide as a σ-Donor Ligand in Coordination Chemistry. *Coord. Chem. Rev.* **1994**, *137*, 483–524.

- (42) Persson, B. N. J.; Tüshaus, M.; Bradshaw, A. M. On the Nature of Dense CO Adlayers. *J. Chem. Phys.* **1990**, *92*, 5034–5046.
- (43) Schilling, C.; Hofmann, A.; Hess, C.; Ganduglia-Pirovano, M. V. Raman Spectra of Polycrystalline CeO₂: A Density Functional Theory Study. *J. Phys. Chem. C* **2017**, *121*, 20834–20849.
- (44) Spanier, J. E.; Robinson, R. D.; Zhang, F.; Chan, S. W.; Herman, I. P. Size-Dependent Properties of CeO₂-y Nanoparticles as Studied by Raman Scattering. *Phys. Rev. B* **2001**, *64*, No. 245407.
- (45) Sartoretti, E.; Novara, C.; Giorgis, F.; Piumetti, M.; Bensaid, S.; Russo, N.; Fino, D. In Situ Raman Analyses of the Soot Oxidation Reaction over Nanostructured Ceria-Based Catalysts. *Sci. Rep.* **2019**, *9*, No. 3875.
- (46) Gendron, F.; Autschbach, J.; Malrieu, J. P.; Bolvin, H. Magnetic Coupling in the Ce(III) Dimer Ce 2 (COT) 3. *Inorg. Chem.* **2019**, *58*, 581–593.
- (47) Yang, Z.; Woo, T. K.; Baudin, M.; Hermansson, K. Atomic and Electronic Structure of Unreduced and Reduced CeO₂ Surfaces: A First-Principles Study. *J. Chem. Phys.* **2004**, *120*, 7741–7749.
- (48) Loschen, C.; Migani, A.; Bromley, S. T.; Illas, F.; Neyman, K. M. Density Functional Studies of Model Cerium Oxide Nanoparticles. *Phys. Chem. Chem. Phys.* **2008**, *10*, 5730–5738.
- (49) Skorodumova, N. V.; Simak, S. I.; Lundqvist, B. I.; Abrikosov, I. A.; Johansson, B. Quantum Origin of the Oxygen Storage Capability of Ceria. *Phys. Rev. Lett.* **2002**, *89*, No. 166601.
- (50) Wasson, M. C.; Otake, K.; Gong, X.; Strathman, A. R.; Islamoglu, T.; Gianneschi, N. C.; Farha, O. K. Modulation of Crystal Growth and Structure within Cerium-Based Metal–Organic Frameworks. *CrystEngComm* **2020**, *22*, 8182–8188.
- (51) Chiang, Y. M.; Lavik, E. B.; Blom, D. A. Defect Thermodynamics and Electrical Properties of Nanocrystalline Oxides: Pure and Doped CeO₂. *Nanostruct. Mater.* **1997**, *9*, 633–642.
- (52) Nagata, T.; Miyajima, K.; Hardy, R. A.; Metha, G. F.; Mafuné, F. Reactivity of Oxygen Deficient Cerium Oxide Clusters with Small Gaseous Molecules. *J. Phys. Chem. A* **2015**, *119*, 5545–5552.
- (53) Chen, H. T.; Chang, J. G. Oxygen Vacancy Formation and Migration in Ce_{1-x}ZrxO₂ Catalyst: A DFT+U Calculation. *J. Chem. Phys.* **2010**, *132*, No. 214702.
- (54) Ziembka, M.; Hess, C. Influence of Gold on the Reactivity Behaviour of Ceria Nanorods in CO Oxidation: Combining Operando Spectroscopies and DFT Calculations. *Catal. Sci. Technol.* **2020**, *10*, 3720–3730.
- (55) Ziembka, M.; Ganduglia-Pirovano, M. V.; Hess, C. Elucidating the Oxygen Storage-Release Dynamics in Ceria Nanorods by Combined Multi-Wavelength Raman Spectroscopy and DFT. *J. Phys. Chem. Lett.* **2020**, *11*, 8554–8559.
- (56) Maciel, C. G.; de Freitas Silva, T.; Profeti, L. P. R.; Assaf, E. M.; Assaf, J. M. Study of CuO/CeO₂ Catalyst with for Preferential CO Oxidation Reaction in Hydrogen-Rich Feed (PROX-CO). *Appl. Catal., A* **2012**, *431*–432, 25–32.
- (57) Mosrati, J.; Abdel-Mageed, A. M.; Vuong, T. H.; Grauke, R.; Bartling, S.; Rockstroh, N.; Atia, H.; Armbruster, U.; Wohlrab, S.; Rabeah, J.; Brückner, A. Tiny Species with Big Impact: High Activity of Cu Single Atoms on CeO₂-TiO₂ Deciphered By Operando Spectroscopy. *ACS Catal.* **2021**, *11*, 10933–10949.
- (58) Muravev, V.; Spezzati, G.; Su, Y. Q.; Parastaev, A.; Chiang, F. K.; Longo, A.; Escudero, C.; Kosinov, N.; Hensen, E. J. M. Interface Dynamics of Pd–CeO₂ Single-Atom Catalysts during CO Oxidation. *Nat. Catal.* **2021**, *4*, 469–478.